# Electronic Supplementary Information

## Stepped copper sites coupling voltage-induced surfactant assembly to achieve efficient $CO_2$ electroreduction to formate

Sicong Qiao,[‡,a] Guikai Zhang,[‡,b] Dong Tian,[*,c] Wenjie Xu,[a] Wei Jiang,[a] Yuyang Cao,[a] Jun Qian,[d] Jing Zhang,[b] Qun He,[*,a] and Li Song[*,a,e]

[a] National Synchrotron Radiation Laboratory, Key Laboratory of Precision and Intelligent Chemistry, School of Nuclear Science and Technology, University of Science and Technology of China, Hefei 230029, China.

[b] Beijing Synchrotron Radiation Facility, Institute of High Energy Physics, Chinese Academy of Science, Beijing 100049, China.

[c] State Key Laboratory of Complex Nonferrous Metal Resources Clean Utilization, Kunming University of Science and Technology, Kunming 650093, China.

[d] High-End Chemicals and Cutting-Edge New Materials Technology Innovation Center of Hefei, East China Engineering Science and Technology Co., LTD., Hefei 230088, China.

[e] Zhejiang Institute of Photonelectronics, Jinhua 321004, China.

[‡]These authors contributed equally to this work.

E-mail: song2012@ustc.edu.cn, hqun@ustc.edu.cn, dong.tian@kust.edu.cn

**Methods**

*Synthesis of $Cu_2O$@Cu.* The $Cu_2O$@Cu was synthesized via an electrochemical etching method. Initially, a Cu foil (10 μm in thickness) was cleaned sequentially under sonication using 0.5 M $H_2SO_4$, deionized water, and ethanol. Electrochemical redox processes were then performed using a conventional three-electrode system, where a 1×1 $cm^2$ Cu foil served as the working electrode, a Pt wire as the counter electrode, and an Ag/AgCl electrode as the reference. The electrolyte solution was Ar-saturated 0.5 M $KHCO_3$. The oxidized Cu foil precursor was obtained by subjecting the electrode to a potential of 3.3 $V_{RHE}$ for 240 seconds. Subsequently, the final $Cu_2O$@Cu precatalyst was produced through further reduction at -0.55 $V_{RHE}$ for 480 seconds.

*Material Characterization.* XRD patterns were collected using a Rigaku TTR III diffractometer equipped with Cu $K_\alpha$ radiation (λ = 1.54178 Å). SEM images were recorded using a Zeiss GeminiSEM 360 microscope. TEM, HRTEM, and EDX mapping images were obtained through a FEI Talos F200X microscope. For TEM tests, the $Cu_2O$@Cu sheet was cut into pieces and immersed in water, followed by sonication for 20 minutes, with the resulting supernatant used for imaging. ATR-IR spectra were obtained through a Thermo Nicolet iN10 spectrometer. In-situ Raman measurements were performed using a Horiba LabRAM HR Evolution spectrometer in 0.5 M $KHCO_3$ with moderate amounts of CTAB. XPS survey spectra were collected using a Thermo ESCALAB 250Xi spectrometer. XPS and AES tests with $Ar^+$ ething were carried out at the Catalysis and Surface Science end-station of the BL11U beamline at the National Synchrotron Radiation Laboratory (NSRL), China. XAFS and DAFS spectra were measured at the 1W1B beamline of the Beijing Synchrotron Radiation Facility (BSRF), China.

All data processing adhered to standard procedures.[1-3]

*Electrochemical Measurements.* Electrochemical $CO_2$RR measurements were conducted using a CHI760E workstation configured with a standard three-electrode system. During these tests, all potentials were carefully calibrated and corrected for resistance compensation. In the H-cell configuration, a free-standing 1×0.5 $cm^2$ $Cu_2O$@Cu served as the working electrode, while a Pt wire and an Ag/AgCl electrode acted as the counter and reference electrodes, respectively. The electrolyte solution was $CO_2$-saturated 0.5 M $KHCO_3$ containing moderate amounts of CTAB. The cathodic and anodic compartments of the cell were separated by a Nafion 117 membrane. Once the CV curves stabilized, chronoamperometry (CA) experiments were performed under applied potentials. Gas products were analyzed using online gas chromatography (GC, Agilent 7890B), and liquid products were quantified by mixing 700 μL of the electrolyte with 500 μL of deuterated water and analyzing the mixture with a $^1H$ nuclear magnetic resonance spectrometer ($^1H$ NMR, Bruker AVANCE III 400).[4,5] Additionally, flow cell tests were conducted in a commercial reactor, also separated by a Nafion 117. In this setup, a 1×0.5 $cm^2$ $Cu_2O$@Cu and a gas diffusion electrode (GDE) were employed as the working electrode, with a Ni foam and an Ag/AgCl used as the counter and reference electrodes, respectively. The electrolyte solution was $CO_2$-saturated 0.5 M $KHCO_3$ containing 0.5 mM CTAB, and the $CO_2$ flow rate was maintained at 30 sccm. To assess the stability, chronopotentiometry (CP) tests were conducted at a constant current density of -40 mA $cm^{-2}$.

*DFT calculations*. Spin-polarized density functional theory (DFT) calculations were carried out using the Vienna ab initio simulation package (VASP) code.[6-8] The generalized gradient approximation of Perdew-Burke-Ernzerhof (PBE) was employed for the electronic exchange

and correlation.[9-11] The plane wave pseudopotential with a kinetic cutoff energy of 400 eV was used through the projector augmented wave (PAW) method.[12,13] The vacuum layer was set to ~15 Å. For the structural optimization, atoms in the bottom two layers were fixed, while all other atoms were released until the force on each ion was smaller than 0.01 eV $Å^{-1}$. The convergence criteria of $1\times10^{-5}$ were chosen. The Brillouin-zone integration was performed using the Monkhorst-Pack grids of 3×3×1 and Methfessel-Paxton smearing of 0.05 eV. In addition, the van der Waals correction was implemented for the weak interaction with the catalyst using the DFT-PBE-D3 method.[11,14] The changes in Gibbs free energies (ΔG) were calculated at 298.15 K with the equation of $\Delta G = \Delta E + \Delta ZPE - T\Delta S$, where ΔE was the binding energy difference of adsorbed species, ΔZPE was the difference of zero-point energy, and TΔS was the entropy contribution.[15-17]

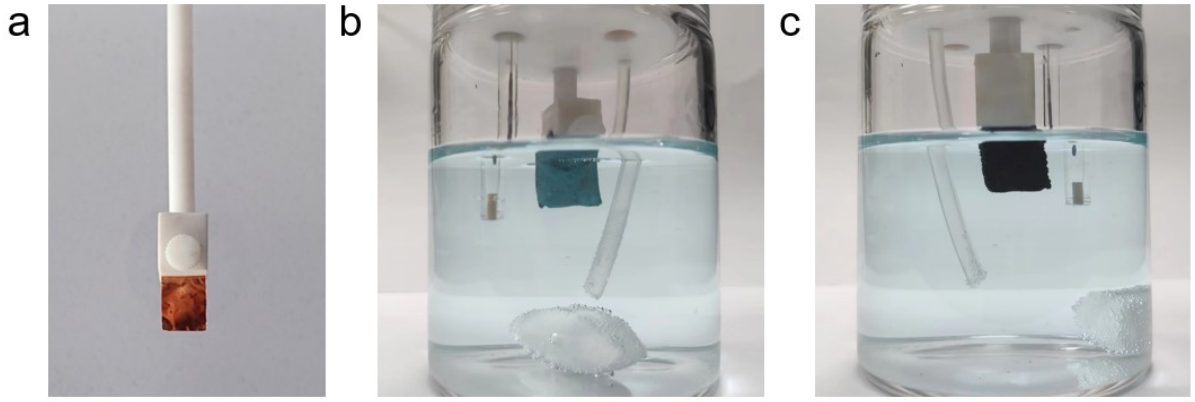


**Fig. S1** Digital photographs of (a) bare Cu foil, (b) oxidized Cu foil, and (c) $Cu_2O$@Cu.

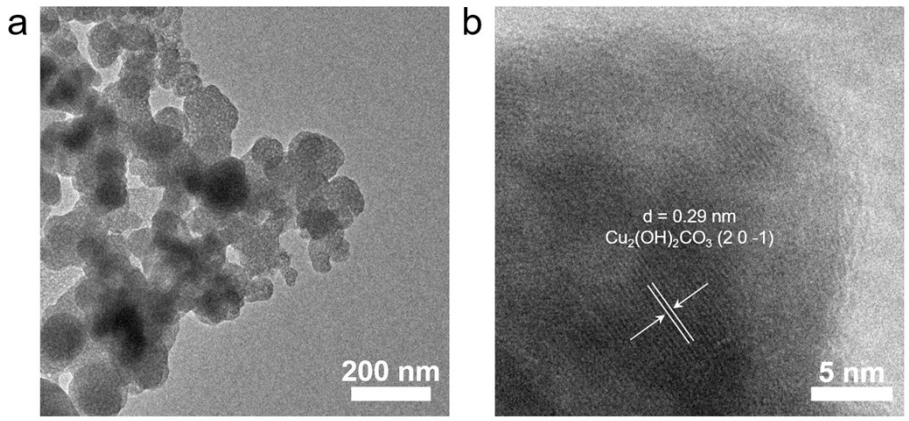


**Fig. S2** (a) TEM and (b) HRTEM images of $Cu_2(OH)_2CO_3$ in the oxidized Cu foil.

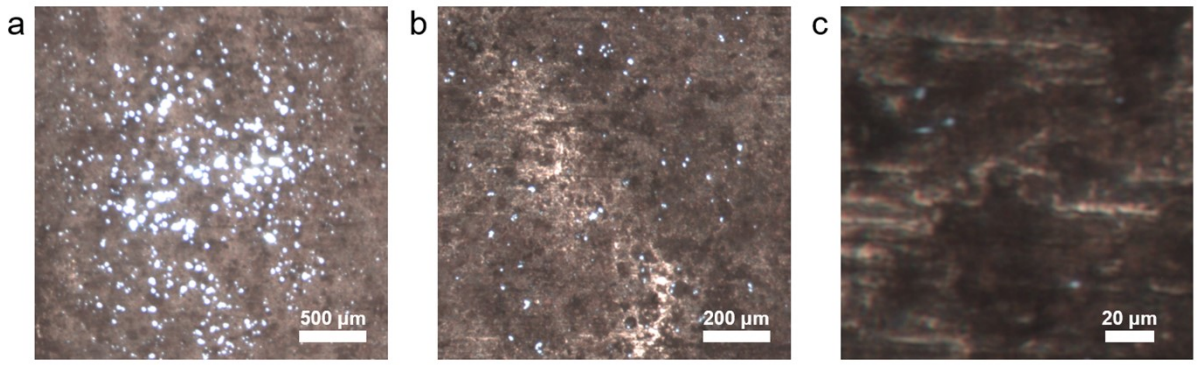


**Fig. S3** (a-c) Digital photographs of $Cu_2O$@Cu.

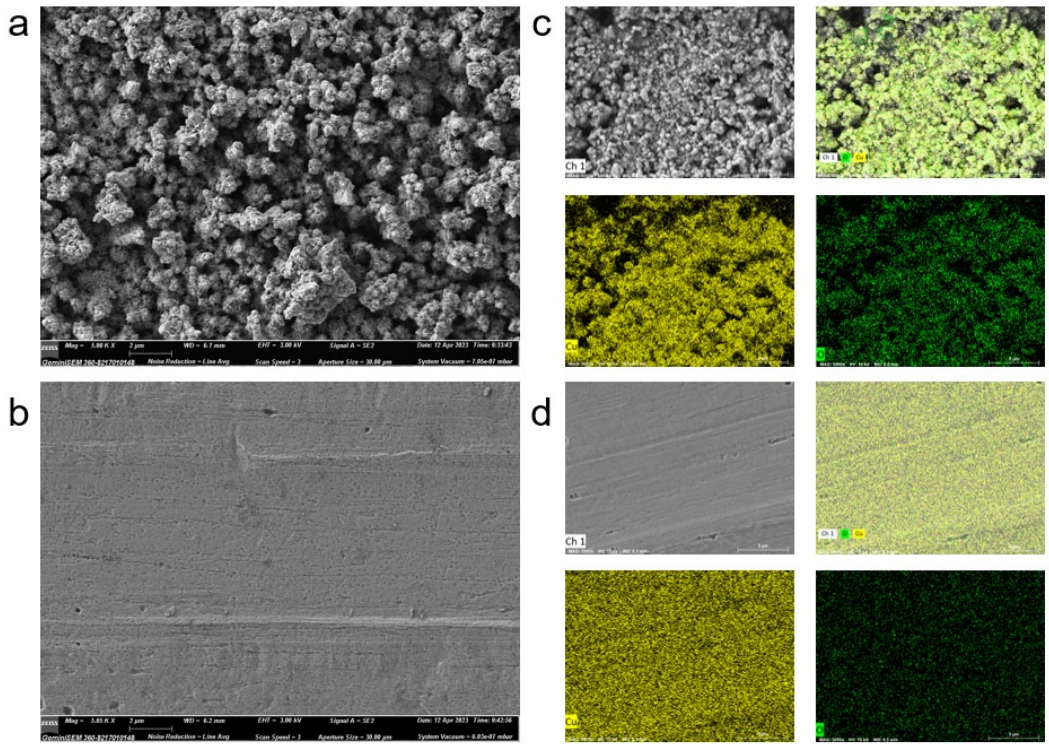


**Fig. S4** (a, b) SEM images of $Cu_2O$@Cu (a) and bare Cu foil (b), respectively. (c, d) Elemental mapping of $Cu_2O$@Cu (c) and Cu foil (d), respectively.

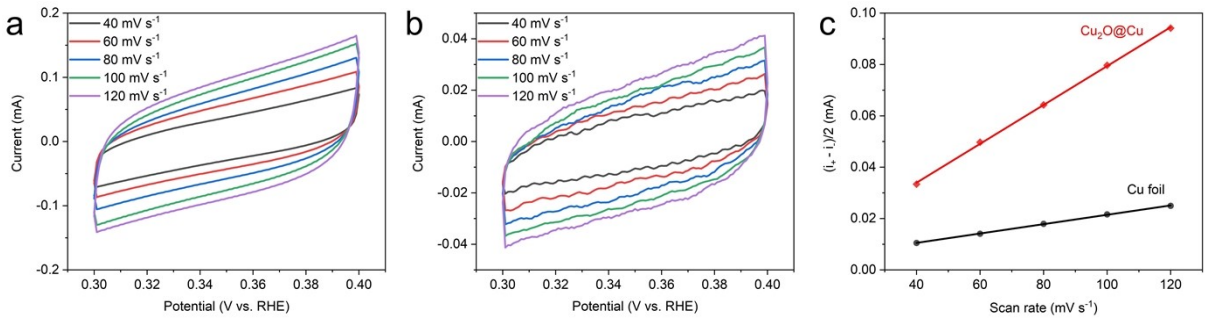


**Fig. S5** (a) CV curves of $Cu_2O$@Cu collected at various scan rates. (b) CV curves of Cu foil collected at various scan rates. (c) Plots of current densities versus scan rates.

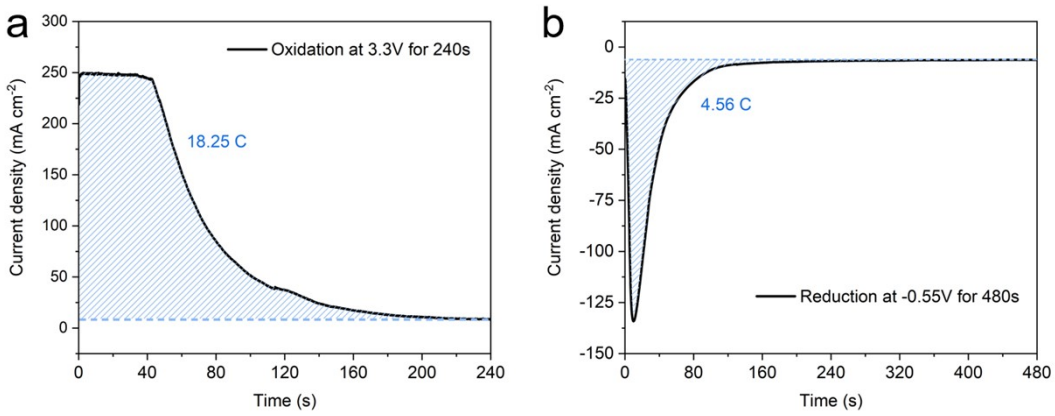


**Fig. S6** (a) The chronoamperometry curve of the electrochemical oxidation of Cu foil. (b) The chronoamperometry curve of the electrochemical reduction of oxidized Cu foil precursor.

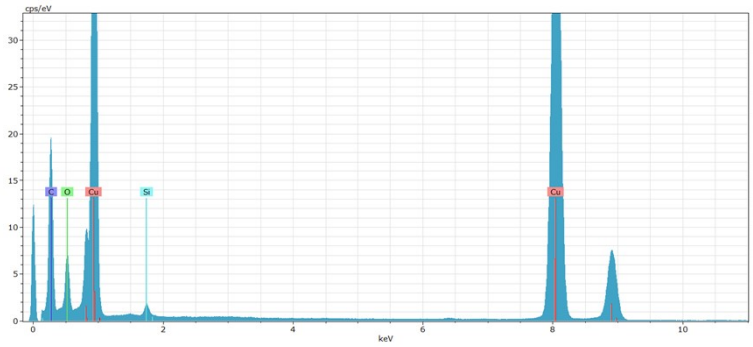


**Fig. S7** The EDX spectrum of $Cu_2O$@Cu.

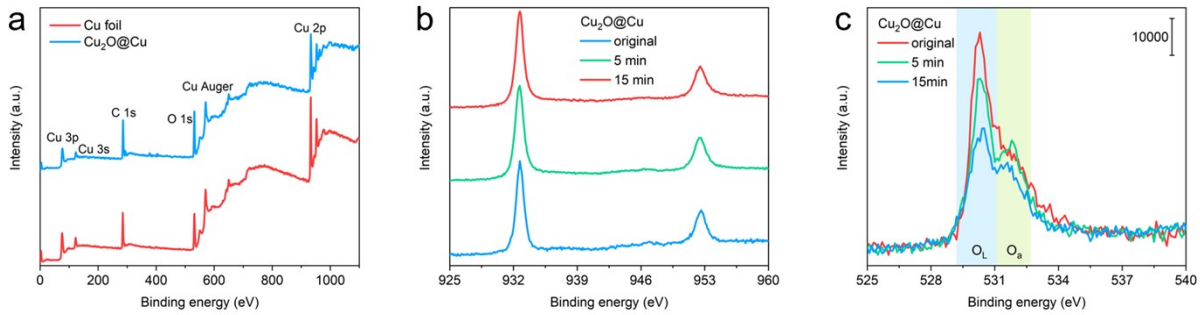


**Fig. S8** (a) XPS survey spectra of Cu foil and $Cu_2O$@Cu. (b, c) Cu 2p (b) and O 1s (c) XPS spectra without and with different durations of $Ar^+$ etching.

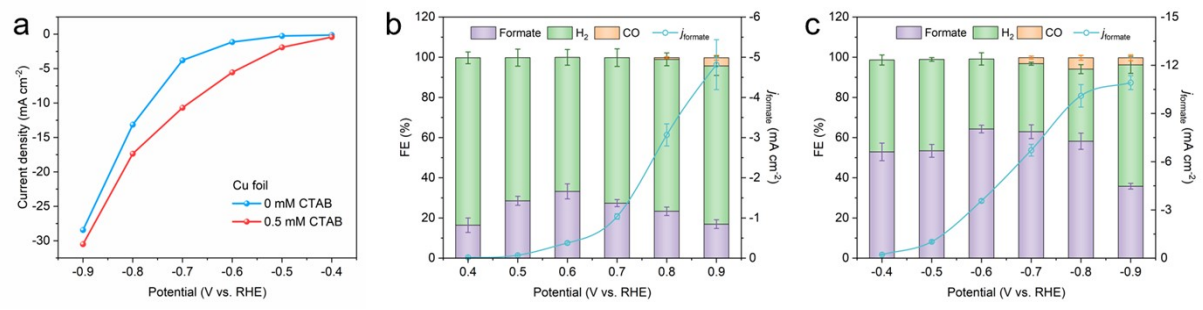


**Fig. S9** (a) Total current densities of Cu foil measured in an H-type cell. (b) $FE_{formate}$ and $j_{formate}$ of Cu foil without 0.5 mM CTAB. (c) $FE_{formate}$ and $j_{formate}$ of Cu foil with 0.5 mM CTAB.

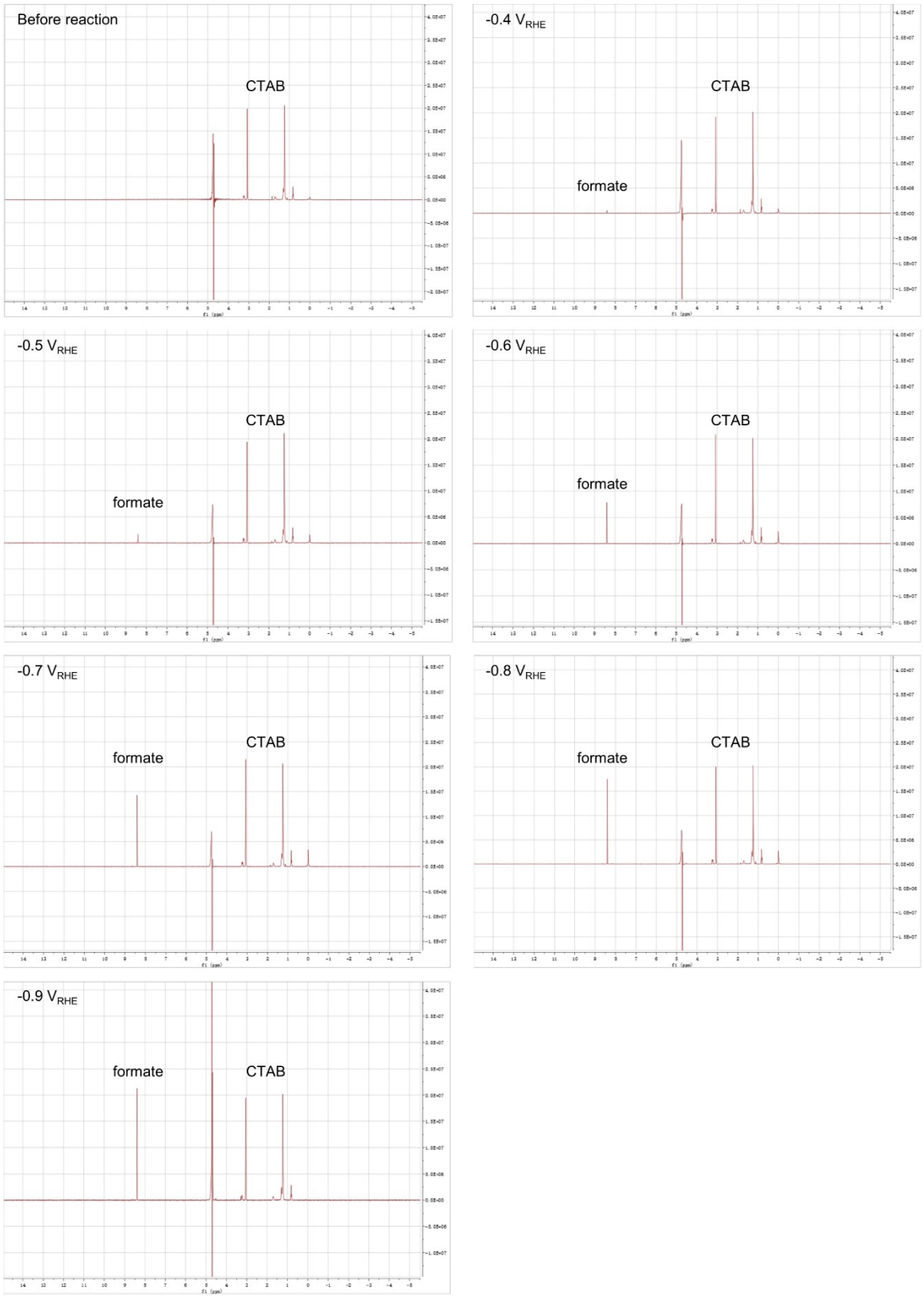


**Fig. S10** $^{1}$H NMR spectra of $Cu_2O$@Cu with 0.5 mM CTAB.

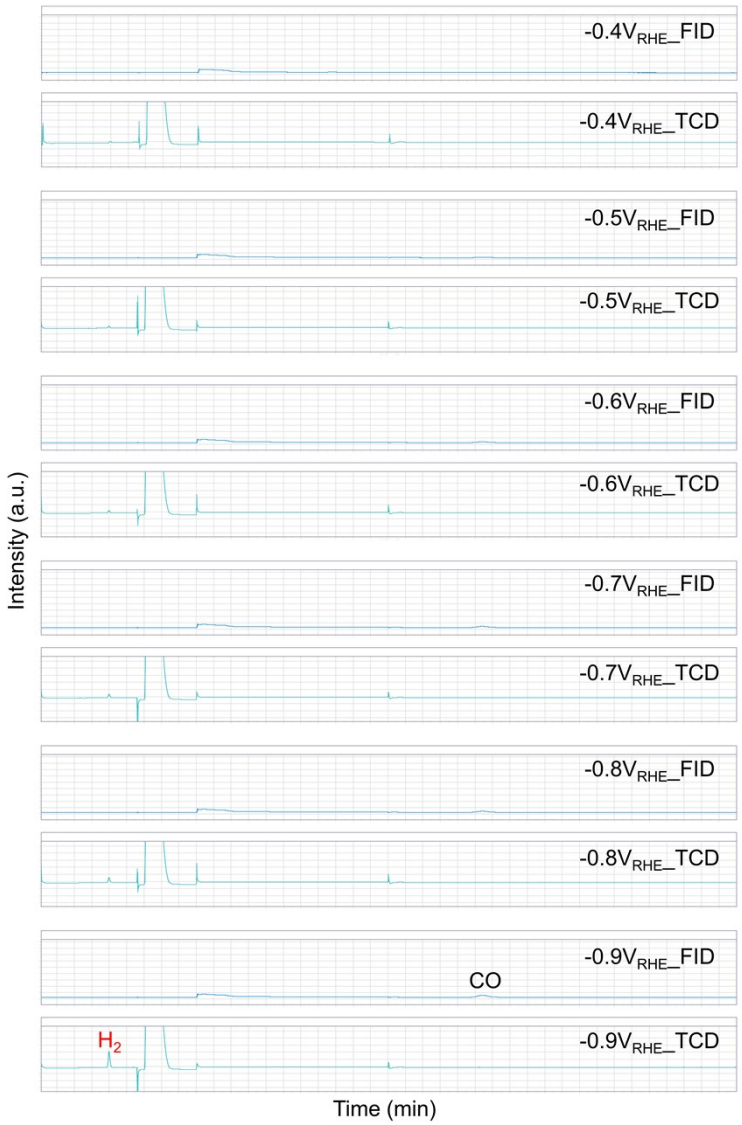


**Fig. S11** GC spectra of $Cu_2O$@Cu with 0.5 mM CTAB.

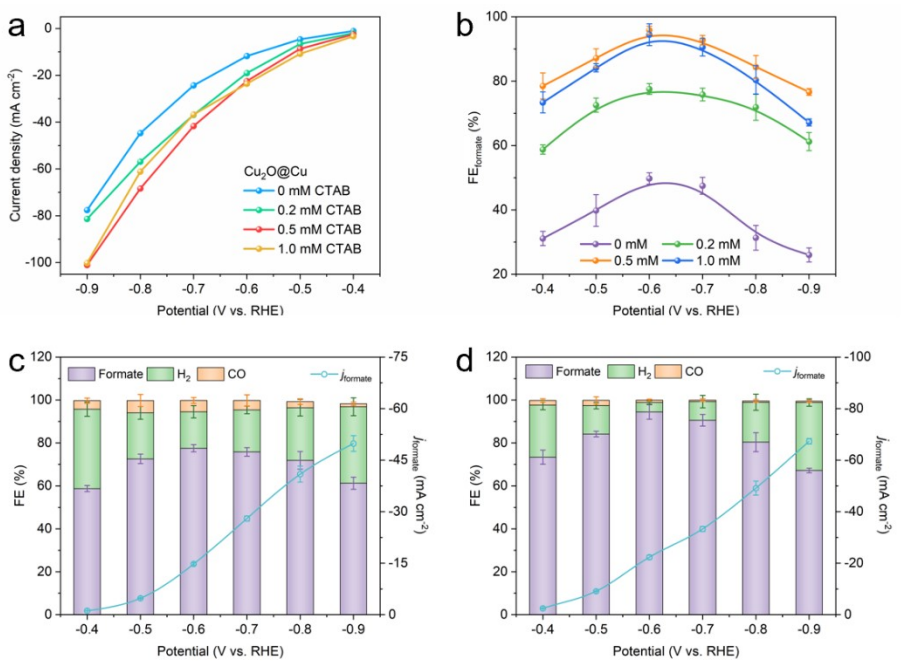


**Fig. S12** (a) Total current densities and (b) $FE_{formate}$ of $Cu_2O$@Cu in an H-type cell. (c) $FE_{formate}$ and $j_{formate}$ of $Cu_2O$@Cu with 0.2 mM CTAB. (d) $FE_{formate}$ and $j_{formate}$ of $Cu_2O$@Cu with 1.0 mM CTAB.

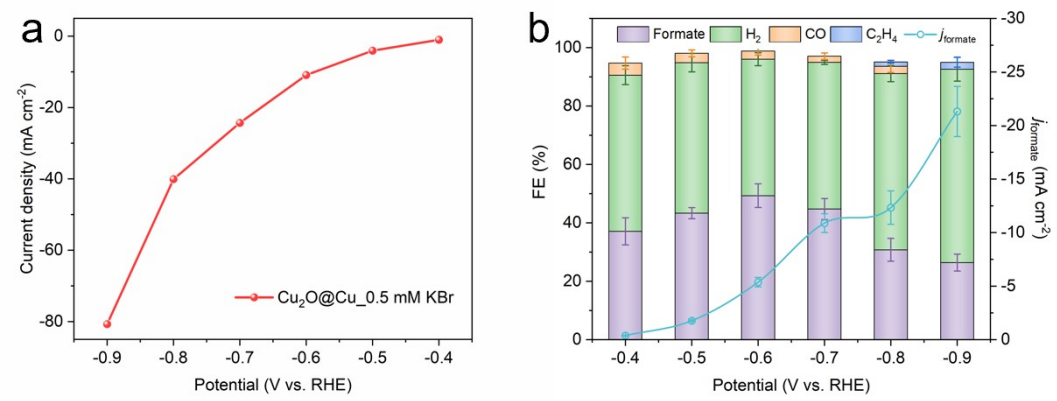


**Fig. S13** (a) Total current densities of $Cu_2O$@Cu in an H-type cell with 0.5 mM KBr as the additive of electrolyte solution. (b) $FE_{formate}$ and $j_{formate}$ of $Cu_2O$@Cu with 0.5 mM KBr.

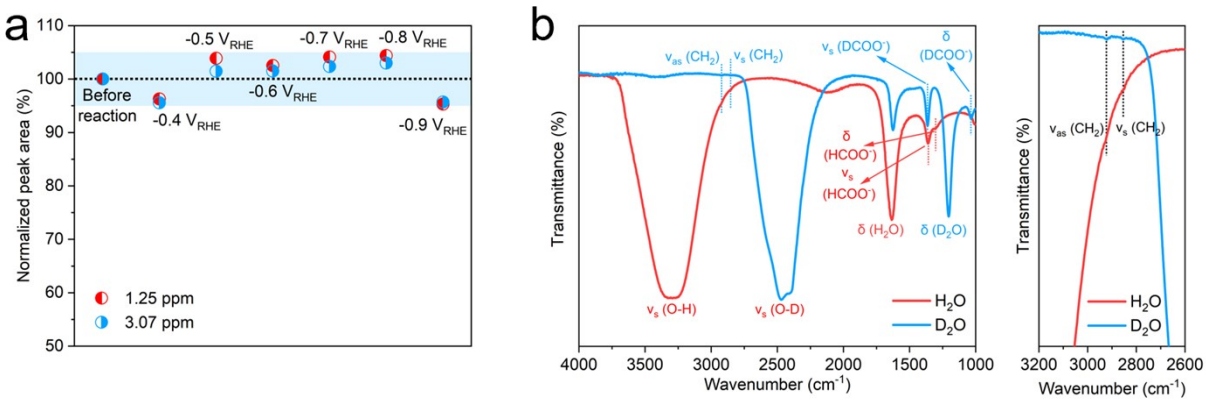


**Fig. S14** (a) $^{1}$H NMR peak areas of CTAB at applied potentials. (b) FTIR spectra of $KHCO_3$ ($H_2O$) and $KHCO_3$ ($D_2O$) electrolyte after $CO_2RR$.

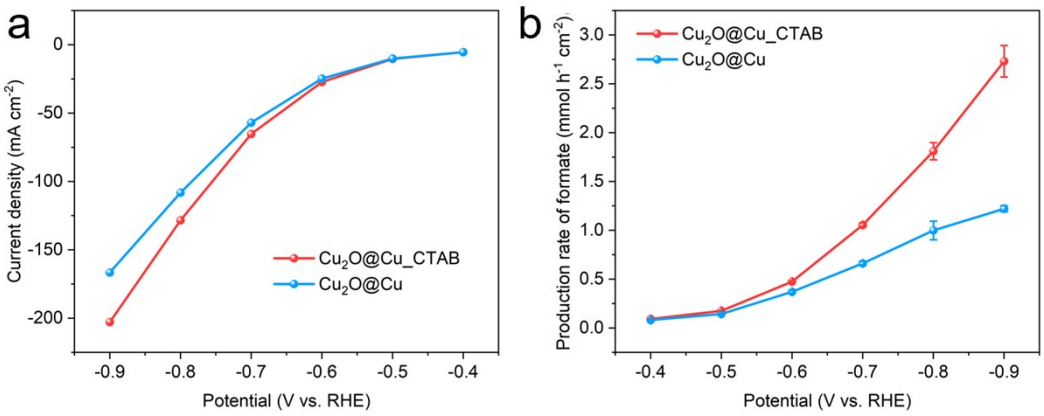


**Fig. S15** (a) Total current densities and (b) production rates of formate in a flow cell without and with 0.5 mM CTAB.

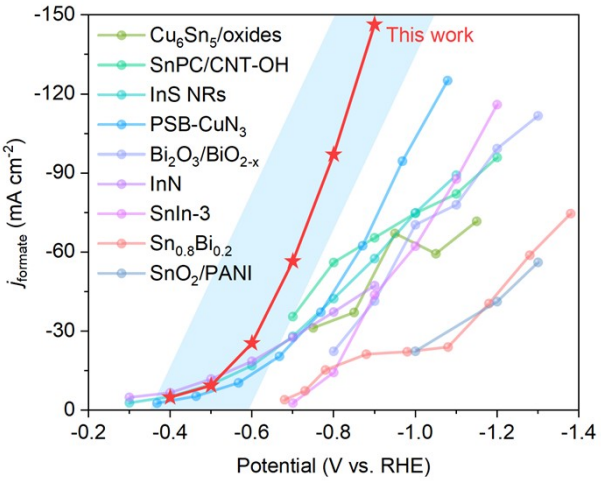


**Fig. S16** Comparison of $j_{formate}$ for various reported catalysts in a flow cell.

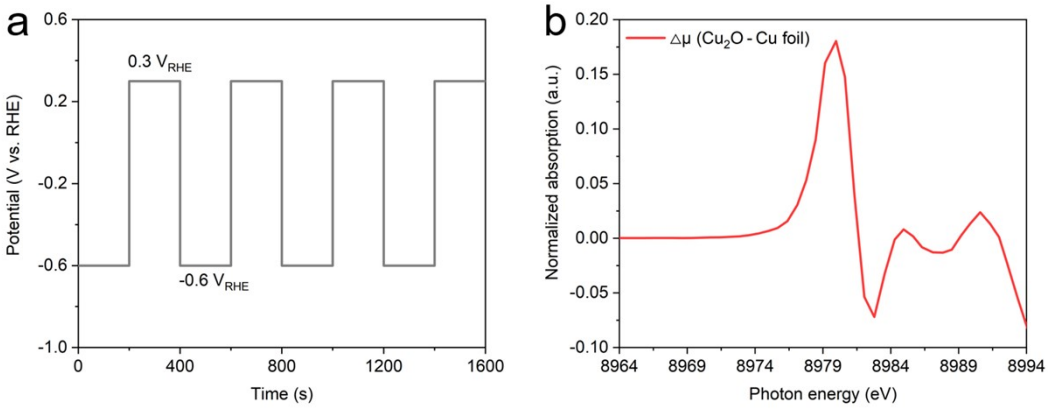


**Fig. S17** (a) The applied potentials during in-situ electrochemical modulating differential XAFS measurements. (b) The differential spectrum of $Cu_2O$ and Cu foil.

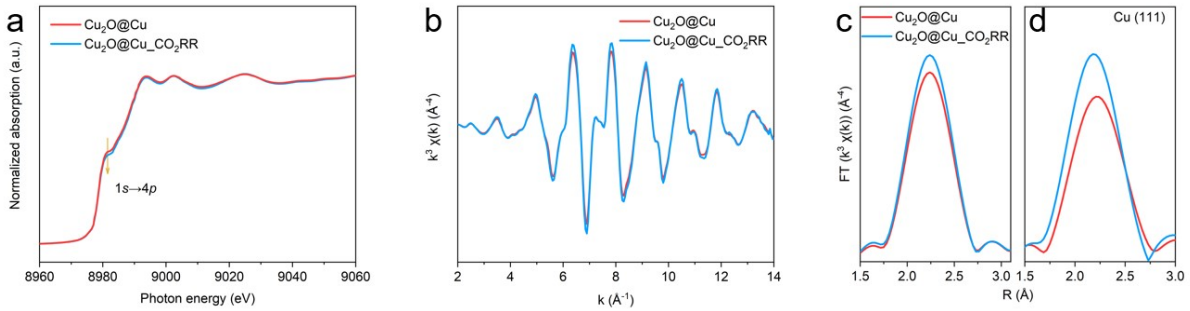


**Fig. S18** (a) Ex-situ XANES spectra of $Cu_2O$@Cu. (b) $k^3$-weighted $k$-space Cu K-edge spectra. (c) Ex-situ FT-EXAFS spectra. (d) Ex-situ Cu(111) FT-EXAFS spectra extracted from DAFS.

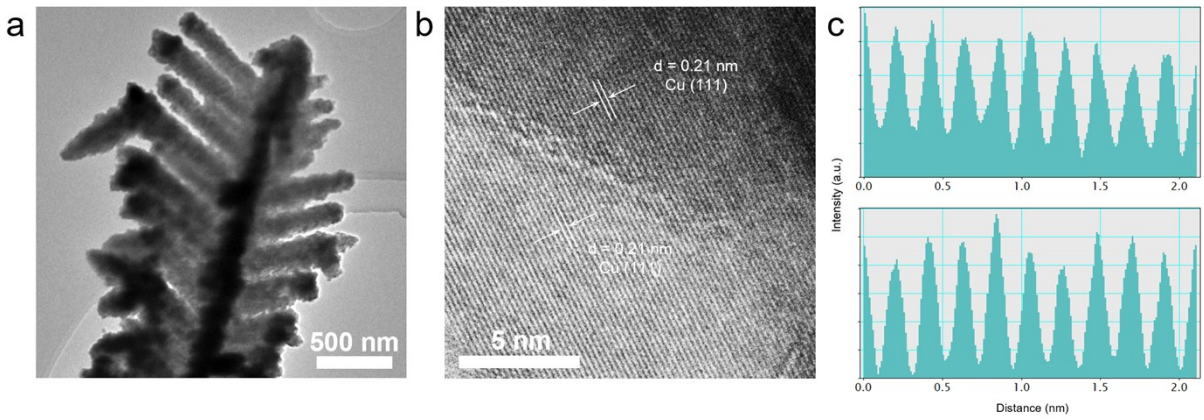


**Fig. S19** (a) TEM image of $Cu_2O$@Cu_$CO_2$RR. (b, c) HRTEM image and corresponding intensity profiles along Cu(111) lattices.

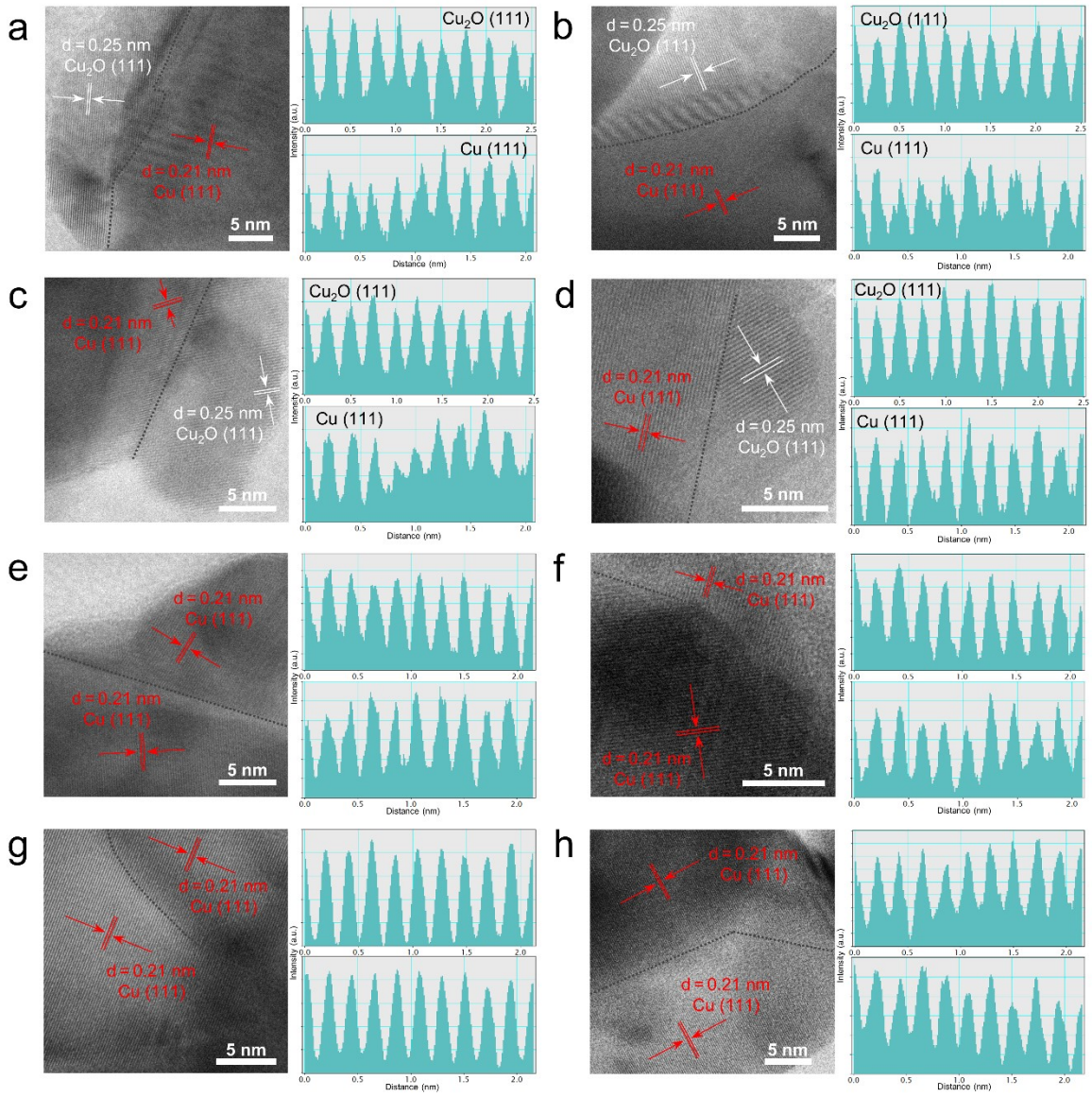


**Fig. S20** Ex-situ HRTEM tests of $Cu_2O$@Cu. (a-d) HRTEM images and corresponding intensity profiles along $Cu_2O$(111) and Cu(111) lattices before $CO_2$RR. (e-h) HRTEM images and corresponding intensity profiles along Cu(111) lattices after $CO_2$RR. In detail, $Cu_2O$@Cu was initially loaded on the Cu TEM grid to observe the morphology of $Cu_2O$@Cu precatalyst. Then, a two-electrode system was assembled using the Cu grid as the cathode and carbon cloth as the anode. After the reduction at -1 mA for 1 hour in $CO_2$-saturated 0.5 M $KHCO_3$, the Cu grid was used to observe the morphology of the resultant catalyst.

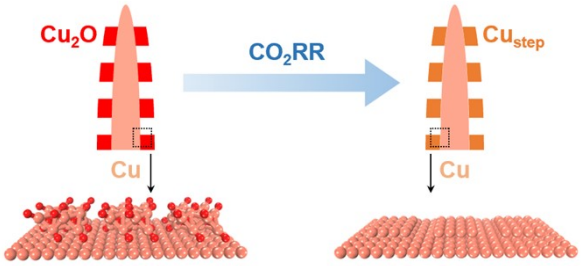


**Fig. S21** Schematic diagram for the formation of $Cu_{step}$ sites.

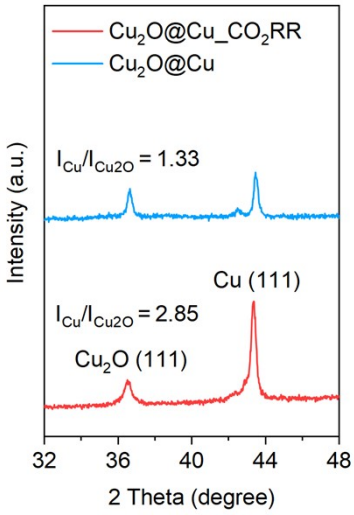


**Fig. S22** Ex-situ XRD spectra of $Cu_2O$@Cu and $Cu_2O$@Cu_$CO_2$RR.

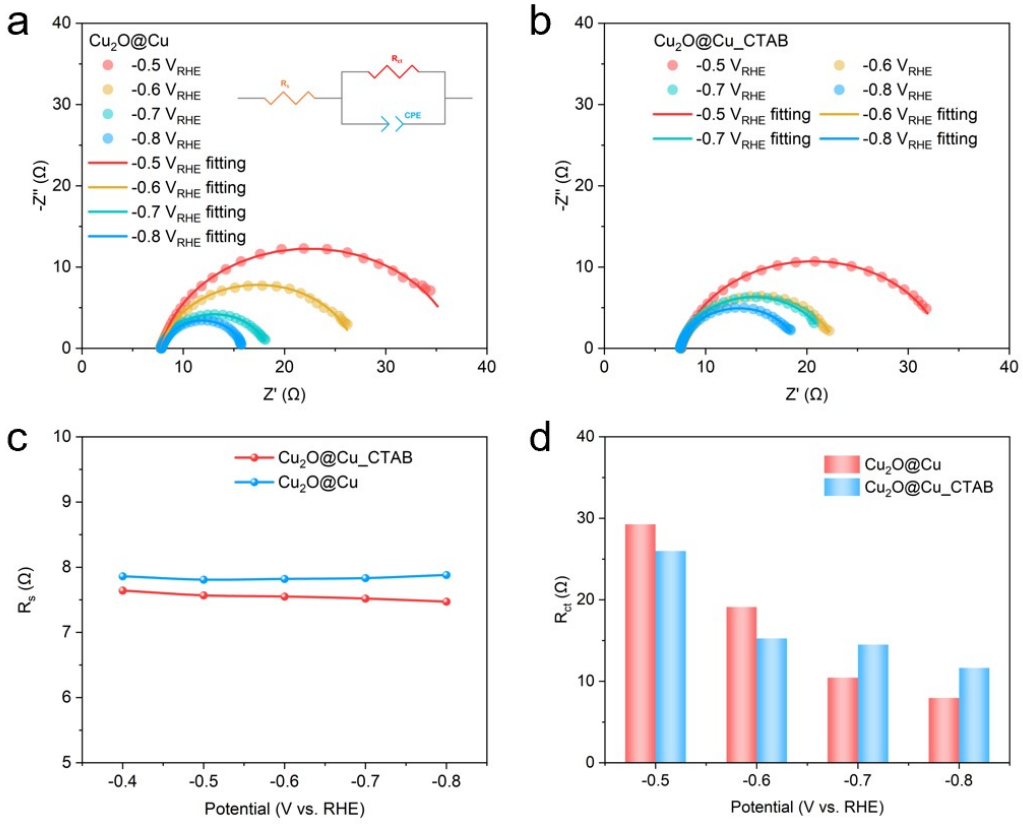


**Fig. S23** (a, b) Nyquist plots without and with CTAB measured at various potentials, respectively. (c, d) Solution resistances (c) and charge transfer resistances (d) without and with CTAB, respectively.

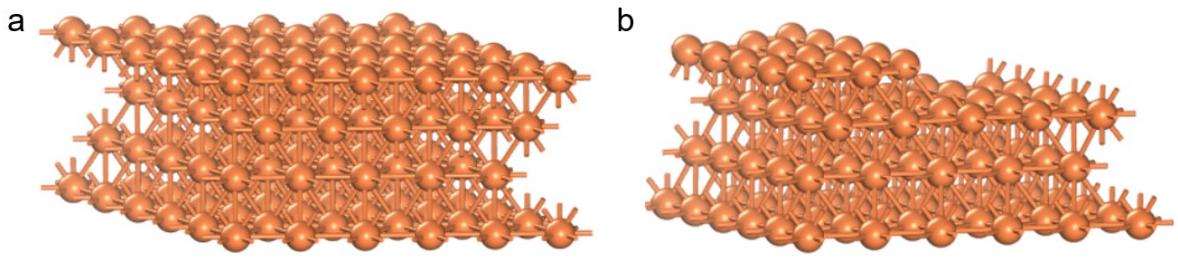


**Fig. S24** (a, b) Schematic diagram of $Cu_{flat}$ (a) and $Cu_{step}$ (b) models.

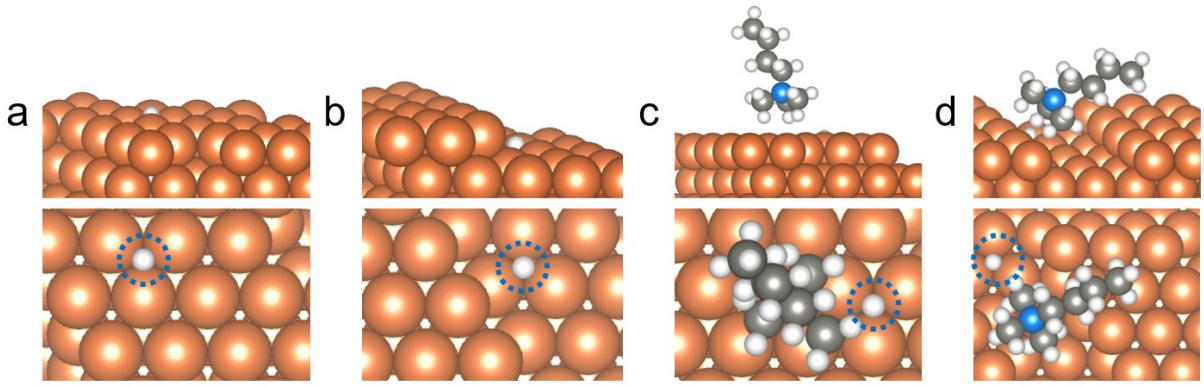


**Fig. S25** (a-d) Schematic diagram of H* adsorbed on $Cu_{flat}$ (a), $Cu_{step}$ (b), $Cu_{flat}$-$BTA^+$ (c), and $Cu_{step}$-$BTA^+$ (d).

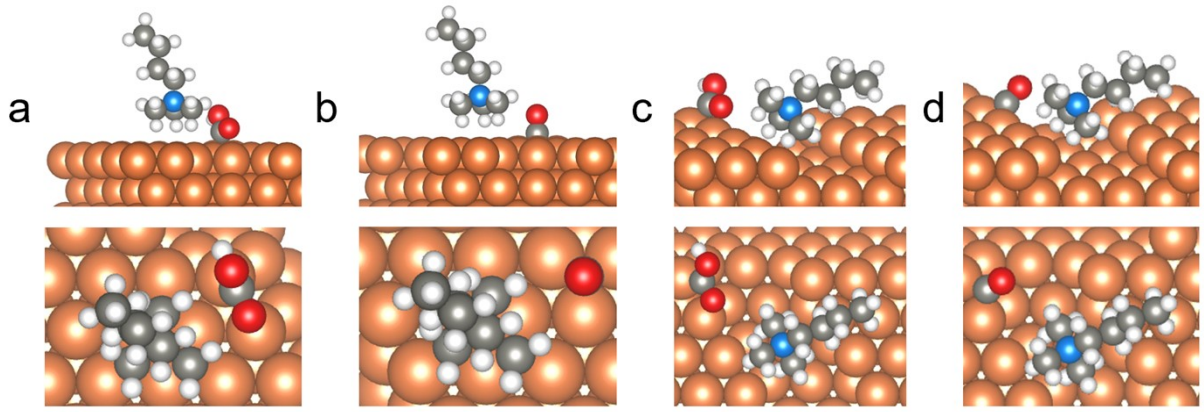


**Fig. S26** (a, b) Schematic diagram of *COOH (a) and *CO (b) adsorbed on $Cu_{flat}$-$BTA^+$. (c, d) Schematic diagram of *COOH (a) and *CO (b) adsorbed on $Cu_{step}$-$BTA^+$.

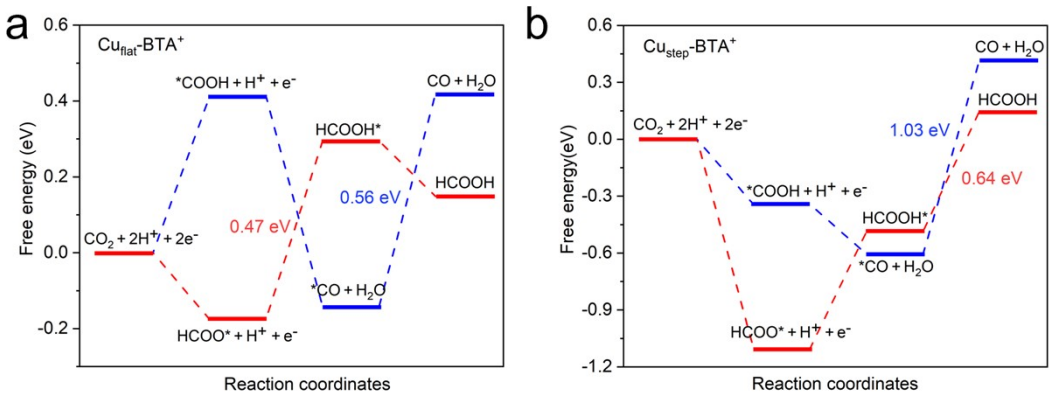


**Fig. S27** (a) Free energy diagrams of $CO_2RR$ on $Cu_{flat}$-$BTA^+$. (b) Free energy diagrams of $CO_2RR$ on $Cu_{step}$-$BTA^+$.

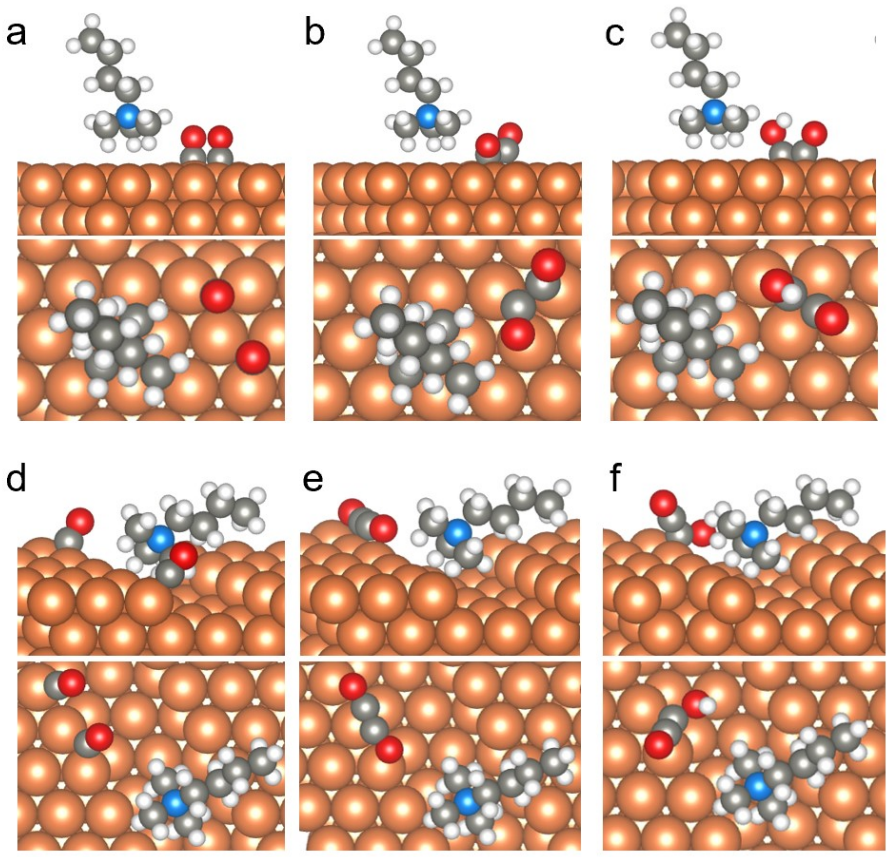


**Fig. S28** (a-c) Schematic diagram of two *CO (a), *OCCO (b), and *OCCHO (c) adsorbed on $Cu_{flat}$-$BTA^{+}$. (d-f) Schematic diagram of two *CO (d), *OCCO (e), and *OCCHO (f) adsorbed on $Cu_{step}$-$BTA^{+}$.

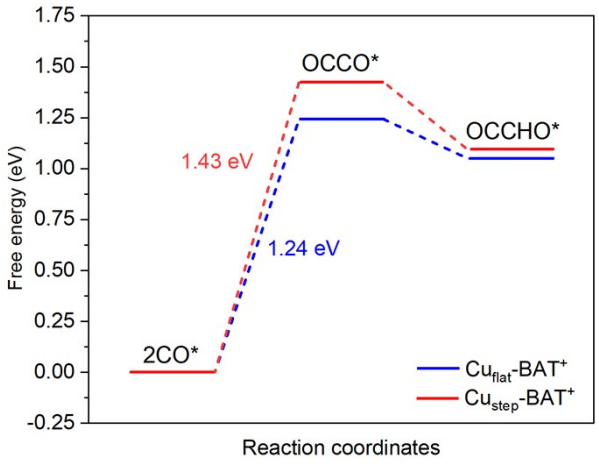


**Fig. S29** Free energy diagrams of C-C coupling on $Cu_{flat}$-$BTA^+$ and $Cu_{step}$-$BTA^+$.

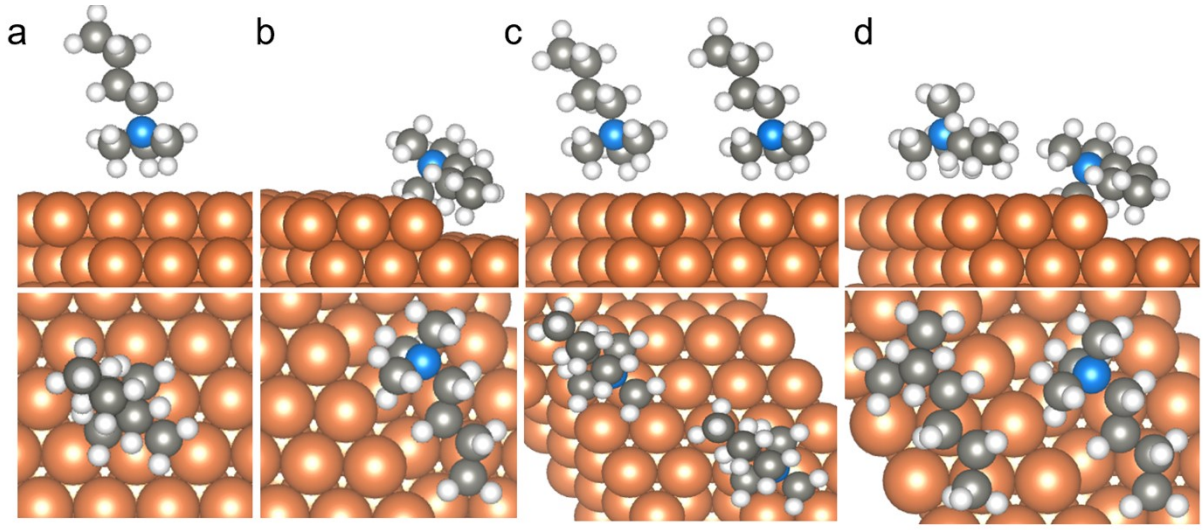


**Fig. S30** (a, b) Schematic diagram of a $BTA^+$ ligand adsorbed on $Cu_{flat}$ (a) and $Cu_{step}$ (b). (c, d) Schematic diagram of two $BTA^+$ ligands adsorbed on $Cu_{flat}$ (c) and $Cu_{step}$ (d).

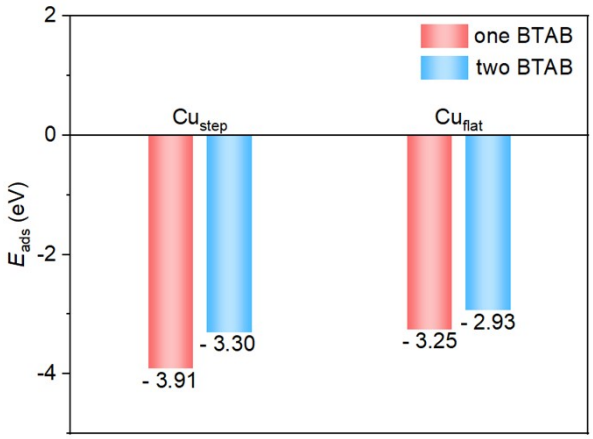


**Fig. S31** The adsorption energies for $BTA^+$ on $Cu_{flat}$ and $Cu_{step}$ sites.

**Table S1.** Comparison of $CO_2RR$ performances in the H-type cell.

| Catalyst | Potential (V vs. RHE) | $j_{formate}$ (mA $cm^{-2}$) | Electrolyte | Reference |
|---|---|---|---|---|
| **$Cu_2O$@Cu** | **-0.90** | **-77.44** | **0.5 M $KHCO_3$** | **This work** |
| $Pb_1Cu$[18] | -0.87 | -27.33 | 0.5 M $KHCO_3$ | *Nat. Nanotechnol.*, 2021, **16**, 1386-1393 |
| Bi-$TiO_2$-700[19] | -1.40 | -18.57 | 0.1 M $KHCO_3$ | *J. Am. Chem. Soc.*, 2023, **145**, 14133-14142 |
| SnPC/CNT-OH[20] | -1.20 | -2.33 | 0.5 M $KHCO_3$ | *J. Am. Chem. Soc.*, 2023, **145**, 7242-7251 |
| PSB-$CuN_3$[21] | -1.13 | -49.78 | 0.5 M $KHCO_3$ | *Nat. Commun.*, 2023, **14**, *6849* |
| In-SAs/NC[22] | -0.95 | -29.01 | 0.5 M $KHCO_3$ | *Angew. Chem. Int. Ed.*, 2020, **59**, 22465-22469 |
| $SnO_2$/$Cu_6Sn_5$/CuO[23] | -0.95 | -23.70 | 0.5 M $NaHCO_3$ | *Adv. Energy Mater.*, 2023, **13**, 2203506 |
| 1T/1H $SnS_2$[24] | -1.11 | -2.97 | 0.1 M $KHCO_3$ | *ACS Nano*, 2023, **17**, 11318-11326 |
| SnIn-3[25] | -1.10 | -34.15 | 0.1 M $KHCO_3$ | *Appl. Catal. B: Environ.*, 2021, **288**, 119979 |
| Co-$PbCO_3$@CNS[26] | -1.10 | -14.76 | 0.5 M $KHCO_3$ | *Appl. Catal. B: Environ.*, 2023, **326**, 122404 |

**Table S2.** Comparison of $CO_2RR$ performances in the flowing cell.

| Catalyst | Potential (V vs. RHE) | $j_{formate}$ (mA $cm^{-2}$) | Electrolyte | Reference |
|---|---|---|---|---|
| **$Cu_2O$@Cu** | **-0.90** | **-146.40** | **0.5 M $KHCO_3$** | **This work** |
| SnPC/CNT-OH[20] | -1.20 | -95.94 | 1 M KOH | *J. Am. Chem. Soc.*, 2023, **145**, 7242-7251 |
| $Sn_{0.80}Bi_{0.20}$@Bi-$SnO_x$[27] | -1.38 | 74.60 | 0.5 M $KHCO_3$ | *Adv. Mater.*, 2020, **32**, 2002822 |
| PSB-$CuN_3$[21] | -1.07 | -125.08 | 0.5 M $KHCO_3$ | *Nat. Commun.*, 2023, **14**, 6849 |
| $SnO_2/Cu_6Sn_5/CuO$[23] | -1.15 | -71.69 | 1 M KOH | *Adv. Energy Mater.*, 2023, **13**, 2203506 |
| $Bi_2O_3/BiO_{2-x}$[28] | -1.3 | -111.42 | 0.5 M $KHCO_3$ | *Nano Lett.*, 2022, **22**, 1656-1664 |
| InN[29] | -0.90 | -47.29 | 1 M KOH | *Nano Lett.*, 2020, **20**, 8229-8235 |
| InS NRs[30] | -1.10 | -89.23 | 1 M KOH | *ACS Appl. Mater. Interfaces*, 2022, **14**, 25257-25266 |
| $SnO_2$/PANI[31] | -1.30 | -56.12 | 2 M $KHCO_3$ | *ACS Appl. Mater. Interfaces*, 2022, **14**, 42144-42152 |
| SnIn-3[25] | -1.20 | -116.00 | 1 M $KHCO_3$ | *Appl. Catal. B: Environ.*, 2021, **288**, 119979 |

**References**

(1) B. Ravel and M. Newville, *J. Synchrotron Radiat.*, 2005, **12**, 537-541.

(2) I. Pickering, M. Sansone, J. Marsch and G. George, *J. Am. Chem. Soc.*, 1993, **115**, 6302-6311.

(3) W. Xu, G. Zhang, H. Shou, J. Zhou, S. Chen, S. Chu, J. Zhang and L. Song, *J. Synchrotron. Radiat.*, 2022, **29**, 1065-1073.

(4) Y. Zhou, Q. Zhou, H. Liu, W. Xu, Z. Wang, S. Qiao, H. Ding, D. Chen, J. Zhu, Z. Qi, X. Wu, Q. He and L. Song, *Nat. Commun.*, 2023, **14**, 3776.

(5) B. Wei, Y. Xiong, Z. Zhang, J. Hao, L. Li and W. Shi, *Appl. Catal. B: Environ.*, 2021, **283**, 119646.

(6) W. Kohn and L. Sham, *Phys. Rev.*, 1965, **140**, A1133-A1138.

(7) P. Hohenberg and W. Kohn, *Phys. Rev.*, 1964, **136**, B864-B871.

(8) G. Kresse and J. Furthmüller, *Phys. Rev. B*, 1996, **54**, 11169-11186.

(9) J. Perdew and Y. Wang, *Phys. Rev. B*, 1992, **46**, 12947-12954.

(10) J. Zheng, G. Ceder, T. Maxisch, W. Chim and W. Choi, *Phys. Rev. B*, 2007, **75**, 104112.

(11) Q. Liang, Y. Zhao, J. Chen, J. Dai, X. Ding, Z. Tong, S. Xie, J. Zhang, Z. Zhou, J. Li, J. Li and Y. Zhou, *Chem. Mater.*, 2022, **34**, 5607-5620.

(12) P. Blöchl, *Phys. Rev. B*, 1994, **50**, 17953-17979.

(13) L. Liang, K. Niu, L. Zhang, J. Tian, K. Zhou, X. Wang, X. Zhang and M. Hong, *ACS Appl. Nano Mater.*, 2021, **4**, 6135-6144.

(14) W. Cao, B. He, C. Liao, L. Yang, L. Zeng and C. Dong, *J. Solid State Chem.*, 2009, **182**, 3353-3357.

(15) R. Xia, D. Tian, S. Kattel, B. Hasa, H. Shin, X. Ma, J. Chen and F. Jiao, *Nat. Commun.*, 2021, **12**, 1949.

(16) Y. Liu, D. Tian, A. Biswas, Z. Xie, S. Hwang, J. Lee, H. Meng and J. Chen, *Angew. Chem. Int. Ed.*, 2020, **59**, 11345-11348.

(17) D. Tian, S. Denny, K. Li, H. Wang, S. Kattel and J. Chen, *Chem. Soc. Rev.*, 2021, **50**, 12338-12376.

(18) T. Zheng, C. Liu, C. Guo, M. Zhang, X. Li, Q. Jiang, W. Xue, H. Li, A. Li, C. Pao, J. Xiao, C. Xia and J. Zeng, *Nat. Nanotechnol.*, 2021, **16**, 1386-1393.

(19) G. Jia, Y. Wang, M. Sun, H. Zhang, L. Li, Y. Shi, L. Zhang, X. Cui, T. Lo, B. Huang and J. Yu, *J. Am. Chem. Soc.*, 2023, **145**, 14133-14142.

(20) Y. Deng, J. Zhao, S. Wang, R. Chen, J. Ding, H. Tsai, W. Zeng, S. Hung, W. Xu, J. Wang, F. Jaouen, X. Li, Y. Huang and B. Liu, *J. Am. Chem. Soc.*, 2023, **145**, 7242-7251.

(21) J. Dong, Y. Liu, J. Pei, H. Li, S. Ji, L. Shi, Y. Zhang, C. Li, C. Tang, J. Liao, S. Xu, H. Zhang, Q. Li and S. Zhao, *Nat. Commun.*, 2023, **14**, 6849.

(22) H. Shang, T. Wang, J. Pei, Z. Jiang, D. Zhou, Y. Wang, H. Li, J. Dong, Z. Zhuang, W. Chen, D. Wang, J. Zhang and Y. Li, *Angew. Chem. Int. Ed.*, 2020, **59**, 22465-22469.

(23) Y. Shi, Y. Wang, J. Yu, Y. Chen, C. Fang, D. Jiang, Q. Zhang, L. Gu, X. Yu, X. Li, H. Liu and W. Zhou, *Adv. Energy Mater.*, 2023, **13**, 2203506.

(24) Y. Kawabe, Y. Ito, Y. Hori, S. Kukunuri, F. Shiokawa, T. Nishiuchi, S. Jeong, K. Katagiri, Z. Xi, Z. Li, Y. Shigeta and Y. Takahashi, *ACS Nano*, 2023, **17**, 11318-11326.

(25) J. Wang, S. Ning, M. Luo, D. Xiang, W. Chen, X. Kang, Z. Jiang and S. Chen, *Appl. Catal. B: Environ.*, 2021, **288**, 119979.

(26) N. Zhang, D. Li, X. Wang, R. Cai, C. Dong, T. Thi Thuy Nga, L. Zhang and D. Yang, *Appl. Catal. B: Environ.*, 2023, **326**, 122404.

(27) Q. Yang, Q. Wu, Y. Liu, S. Luo, X. Wu, X. Zhao, H. Zou, B. Long, W. Chen, Y. Liao, L. Li, P. Shen, L. Duan and Z. Quan, *Adv. Mater.*, 2020, **32**, 2002822.

(28) X. Feng, H. Zou, R. Zheng, W. Wei, R. Wang, W. Zou, G. Lim, J. Hong, L. Duan and H. Chen, *Nano Lett.*, 2022, **22**, 1656-1664.

(29) A. Zhang, Y. Liang, H. Li, B. Zhang, Z. Liu, Q. Chang, H. Zhang, C. Zhu, Z. Geng, W. Zhu and J. Zeng, *Nano Lett.*, 2020, **20**, 8229-8235.

(30) Y. Zhang, J. Lan, F. Xie, M. Peng, J. Liu, T. Chan and Y. Tan, *ACS Appl. Mater. Interfaces*, 2022, **14**, 25257-25266.

(31) D. Sassone, J. Zeng, M. Fontana, M. Farkhondehfal, C. Pirri and S. Bocchini, *ACS Appl. Mater. Interfaces*, 2022, **14**, 42144-42152.